

Resistive AC-Coupled Silicon Detectors: principles of operation and first results from a combined analysis of beam test and laser data

M. Tornago^{1 a,b}, R. Arcidiacono^{b,c}, N. Cartiglia^b, M. Costa^{a,b},
M. Ferrero^{b,c}, M. Mandurrino^b, F. Siviero^{a,b}, V. Sola^b, A. Staiano^b,
A. Apresyan^d, K. Di Petrillo^d, R. Heller^d, S. Los^d,
G. Borghi^{f,g}, M. Boscardin^{f,g}, G-F Dalla Betta^{e,f}, F. Ficorella^{f,g},
L. Pancheri^{e,f}, G. Paternoster^{f,g}
H. Sadrozinski^{h,i}, A. Seiden^{h,i}

^(a) *Università degli Studi di Torino, Italy*

^(b) *INFN Torino, Italy*

^(c) *Università degli Studi del Piemonte Orientale*

^(d) *Fermi National Accelerator Laboratory, Batavia, USA*

^(e) *Università degli Studi di Trento, Italy*

^(f) *INFN-TIFPA, Trento, Italy*

^(g) *Fondazione Bruno Kessler, Trento, Italy*

^(h) *University of California, Santa Cruz*

⁽ⁱ⁾ *Santa Cruz Institute for Particle Physics*

Abstract

This paper presents the principles of operation of Resistive AC-Coupled Silicon Detectors (RSDs) and measurements of the temporal and spatial resolutions using a combined analysis of laser and beam test data. RSDs are a new type of n-in-p silicon sensor based on the Low-Gain Avalanche Diode (LGAD) technology, where the n^+ implant has been designed to be resistive, and the read-out is obtained via AC-coupling. The truly innovative feature of RSD is that the signal generated by an impinging particle is shared isotropically among multiple read-out pads without the need of floating electrodes or an external magnetic field. Careful tuning of the coupling oxide thickness and the n^+ doping profile is at the basis of the successful functioning of this device. Several RSD matrices with different pad-pitch geometries have been

¹email: marta.tornago@edu.unito.it

extensively tested with a laser set-up in the Laboratory for Innovative Silicon Sensors in Torino, while a smaller set of devices have been tested at the Fermilab Test Beam Facility with a 120 GeV/c proton beam. The measured spatial resolution ranges between $2.5 \mu\text{m}$ for 70-100 pad-pitch geometry and $17 \mu\text{m}$ with 200-500 matrices, a factor of 10 better than what is achievable in binary read-out ($\text{bin size}/\sqrt{12}$). Beam test data show a temporal resolution of $\sim 40 \text{ ps}$ for 200- μm pitch devices, in line with the best performances of LGAD sensors.

Keywords: 4D tracking, AC-coupled detectors, LGAD

1. Introduction

AC-Coupled Low Gain Avalanche Diodes (AC-LGADs) [1] are a new generation of silicon devices optimized for high-precision 4D tracking and conceived for experiments at future colliders. They are n-in-p sensors based on the LGAD technology with two additional key features (Figure 1): the AC-coupling of the read-out, occurring through a dielectric layer, and a continuous resistive n^+ implant. Given the presence of the resistive n^+ layer, AC-LGADs are called Resistive Silicon Detectors (RSD). RSD devices are provided with one continuous gain layer and the read-out segmentation is obtained simply by the position of the AC pads; therefore, this design allows to reach 100% fill-factor.

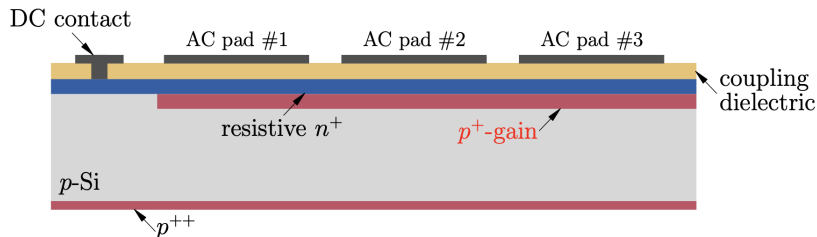


Figure 1: Cross-section of RSDs internal structure: their properties are based on the combination of a resistive n^+ layer and a coupling dielectric oxide, allowing a local AC-coupling.

The remarkable feature of this design is that it leads naturally to signal sharing among pads. Internal signal sharing, in combination with internal gain, opens a new avenue for high precision tracking without relying only

on shrinking the pitch: a position resolution of $\sim 5 \mu m$ is achieved with 200- μm pitch combining the signals from several pads. Instead of focusing on how to design the smallest possible pixel, the RSD design focuses on how to maximize the uniformity of signal sharing and to find the right balance between signal sharing, gain, noise, and reconstruction.

The first RSD production [3, 4] has been manufactured in 2019 by the Fondazione Bruno Kessler. The batch includes 15 wafers, 11 Si-on-Si and 4 epitaxial, with varying n^+ , gain and p-stop doping profiles, and different oxide thicknesses. Each wafer contains several devices with different geometries; the ones used for the measurements presented in this paper are square matrix sensors with a varying number of pads, pitch and pad size.

2. RSD signal properties

Signal formation in RSDs happens in three phases [2].

- (i) In the first one, the drifting e/h pairs produce a direct charge induction on the n^+ conductive implant, similar to a standard LGAD. This initial signal is not seen on the AC-metal pads, unless the metal pad is directly above the impact point.

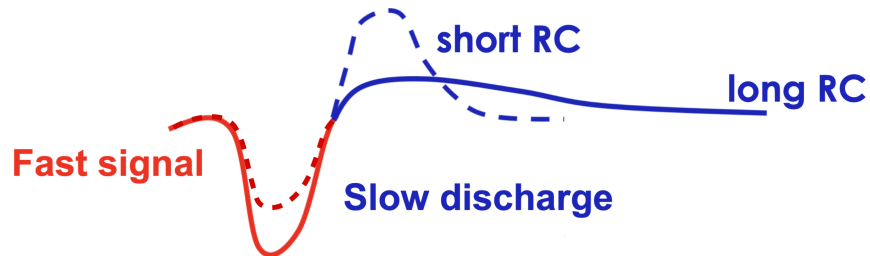


Figure 2: A typical signal generated by an RSD device, characterized by a first fast negative lobe, identical to the signal of an equivalent DC LGAD, and a slow positive lobe by which the AC pad discharges.

- (ii) The signal spreads toward ground on the n^+ layer. The AC metal pads, grounded via the readout electronics, offer to fast signals a path to ground with an resistance far lower than that provided by the n^+ resistive sheet. For this reason, the fast signal (about 1 ns for 50- μm thick sensor) becomes visible on the AC pads, charging the capacitors

formed by the AC metal pads and the n^+ layer. The signal in the AC pads is seen with a delay that increases with distance from the impact point. If the metal pad is right above the impact point, there is no delay. Signal sharing in AC-LGADs happens on the surface of the n^+ layer and does not require long drift lines. This mechanism enables to combine charge sharing and thin detectors. This second phase generates the first lobe of the signal, identical to the one created in an equivalent DC LGAD, as shown in Figure 2.

- (iii) In the last step, the AC pads discharge, generating the second lobe of the signal, with opposite polarity with respect to the first one. The shape of this lobe depends on the resistance to ground R and the pad capacitance C , the RC time constant. Systems with a small RC will have signals with a larger and shorter positive lobe since they need to discharge the same amount of charge in a shorter time. The value of the RC time constant affects also the first lobe: if the RC is too short, the first lobe will be smaller due to ballistic deficit.

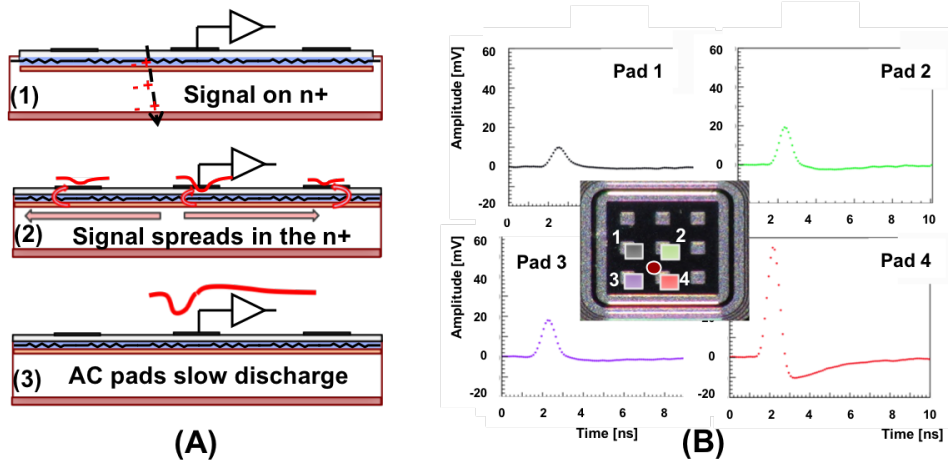


Figure 3: Sketch of the three phases of RSD signals formation (A); example of signal sharing (B): four AC pads see a signal for a hit position corresponding to the red point on the RSD picture.

Figure 3 in (A) shows a sketch describing the three phases of signal formation, while in (B) the signals seen on 4 pads for a laser signal shot at the red position.

3. RSD Reconstruction Models

Extensive studies with a laser setup have been performed in the Laboratory for Innovative Silicon Sensors in Torino, using several RSD matrices with varying pitch and pad size. The main objectives of these measurements were the study of the signal formation and the measurement of the spatial and temporal resolutions as a function of the RSD pitch and pad size.

3.1. RSD Master Formulas: Logarithmic Attenuation Model

In RSDs, a hit generates signals on multiple pads. This can be explained by comparing an RSD to a current divider: in a current divider, the current in a given branch is:

$$I_i = \frac{\frac{1}{Z_i}}{\sum_1^n \frac{1}{Z_i}}, \quad (1)$$

where I_i is the current in the branch i and Z_i the resistance. In an RSD, the situation is very similar, as represented in Figure 4 (left), with the branches of the divider being the resistances of the triangular resistive surface connecting the impact point to each of the neighboring pads. As the signal travels from the hit point to the pad, it spreads over a larger area: the resistance Z_i seen by a signal does not scale linearly with distance (Figure 4 right). Specifically, the resistance per unit length decreases as a function of the distance r as:

$$Z \propto \frac{1}{\alpha} \frac{1}{2\pi r}. \quad (2)$$

where α is the angle of view.

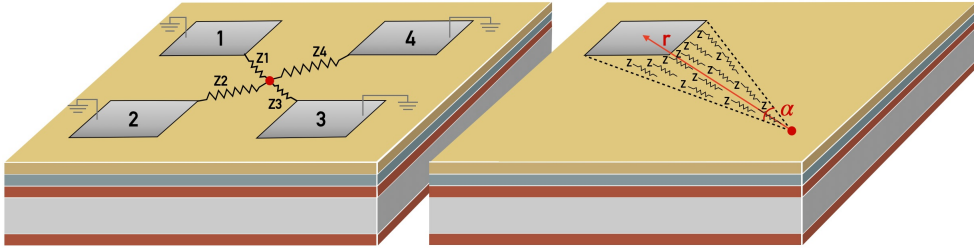


Figure 4: Sketch of an RSD, with the resistances seen by a signal while propagating.

Therefore, the expression for the resistance seen by a signal propagating up to a distance d is:

$$Z = \frac{2\pi}{\alpha} \int_1^d \frac{1}{2\pi r} = \frac{\ln(d)}{\alpha}. \quad (3)$$

Combining Equation (1) with Equation (3), it is possible to calculate how a signal is shared among pads:

$$F_i(\alpha_i, d_i) = \frac{\frac{\alpha_i}{\ln(d_i)}}{\sum_i^n \frac{\alpha_i}{\ln(d_i)}}, \quad (4)$$

where F_i is the fraction of the total signal amplitude seen on the pad i , d_i the distance from the hit point to the pad i metal edge, and α the pad i angle of view. The signal seen on a pad depends on the relative resistance of its path to all the other paths, and not on its absolute value. For this reason, this formula predicts without any free parameter how a signal is shared among pads for every RSD geometry, n^+ resistivity, and dielectric thickness.

This formulation allows to highlight some properties of signals in RSDs:

- the signal seen by a pad depends on how many and how close the other pads are,
- the number of pads that record a signal depends on the hit location
- if the hit is located on a metal pad, and the metal size is large enough (more than about $15 \times 15 \mu m^2$), the signal is almost completely absorbed by a single pad since the resistance to reach that pad is zero,
- a floating pad does not contribute to charge sharing, as the resistance to ground is infinite,
- the sum of all the recorded signals is constant.

Since the n^+ layer is resistive, there is a delay between the hit time and when the signal is formed on the pad. This delay is proportional to the value of the resistance, evaluated by Equation (3), and to the value of the system capacitance. The arrival time on a pad of a signal generated by a particle impinging at a distance d with an angle of view α is shown in Equation (5):

$$t(d, \alpha) = t_0 + \gamma \frac{\log(d)}{\alpha}, \quad (5)$$

where $t(d, \alpha)$ is the time of the signal on the pad, t_0 is the hit time, and γ is the delay factor that can be extracted from experimental data.

We call Equations (4) and (5) the RSD Master Formulas (MFs): they allow to calculate the fraction of the signal seen and its delay.

3.2. Linear Attenuation Model

In order to assess the validity of the MFs, we also developed a second model. This model, the *linear attenuation* model (LA), assumes that the signal on a pad decreases linearly with the distance from the hit point and increases linearly with the angle of view [7]. In the LA model, the fraction of the total signal seen by a pad is given by:

$$F_i(d_i, \alpha_i) = \frac{[1 - \beta * d_i] * \alpha_i}{\sum_i^n [1 - \beta * d_i] * \alpha_i}, \quad (6)$$

where d_i is the distance from the pad metal edge, α_i the angle of view, and β is the attenuation factor. In the LA model, the tunable parameter β is determined from data. The LA model Equation for the time delay also has a linear dependence on the hit distance:

$$t(d) = t_0 + \zeta * d, \quad (7)$$

where ζ is the delay parameter for this model.

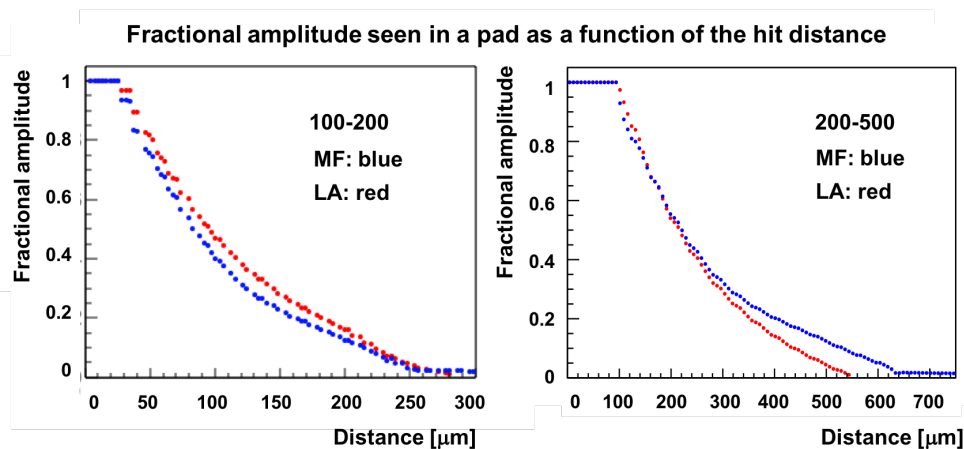


Figure 5: Fraction of the total signal as a function of the hit distance from the center of the AC pads for the Master Formula (blue) and the LA model (red), plotted for the 100-200 and 200-500 pad-pitch geometry.

In the studies presented in this paper, the LA model will be tuned for each geometry to obtain the most accurate position response and it will be used to benchmark the MF model. Figure 5 illustrate an example of this comparison. The plot shows the fraction of the amplitude seen in a pad as a

function of its distance from the hit position as predicted by the MF (in blue) and by the LA model (in red) for the 100-200 and 200-500 geometries. The MF and the LA-tuned predictions are very similar for the smaller geometries, while they differ at large distances in the 200-500 case.

3.3. Position reconstruction

The MF and the LA models allow predicting how a signal is shared among several pads. In this way, a point on the RSD surface is uniquely identified by the relative amplitudes seen by the nearby pads. Exploiting this remarkable property, the location of the hit point can be identified very accurately using the signals measured on several pads. Figure 6 shows an example of the amplitude seen in a given pad as a function of the hit position according to the RSD master formulas (assuming a total amplitude of 120 mV).

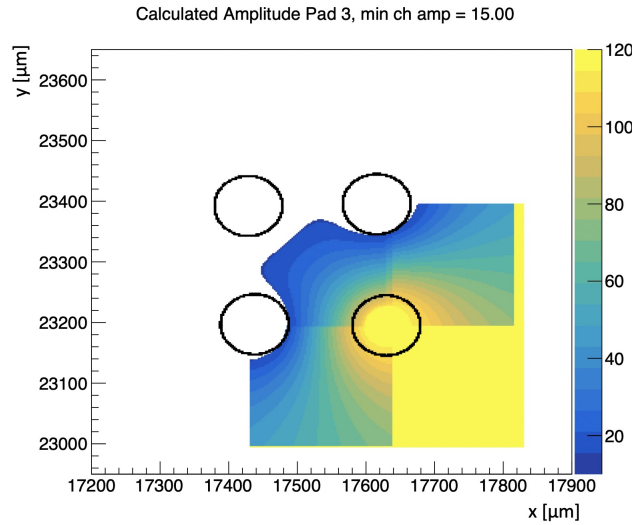


Figure 6: Amplitude map for one AC pad calculated with the RSD Master formulas.

- The total signal A_{tot} amplitude is calculated as the sum of the amplitudes $A[i]$ seen in all active pads, $A_{tot} = \sum_i A[i]$, with $A[i]$ larger than the chosen threshold;
- The fraction of the total amplitude seen in each pad is calculated as $(A[i]/A_{tot})_{Meas}$;

- This set of fractions is compared with the predicted fraction (using either MF or LA) in each x-y point. The hit position is the bin that minimizes the following chi-square:

$$\chi^2 = \sum_i \left[\left(\frac{A[i]}{A_{tot}} \right)_{Meas} - \left(\frac{A[i]}{A_{tot}} \right)_{Calc} \right]^2; \quad (8)$$

- The accuracy can be increased by performing a local interpolation around the minimum.

This iterative procedure locates the particle impinging point, according to the MF or LA model, as the position of the bin that best reproduces the measured share of amplitudes among pads.

3.4. Design optimization

As seen in the previous paragraph, signal sharing is germane to the RSD design, and this property is used in the location of the hit position. However, how the signal is shared depends upon many factors such as the hit position, the RSD geometry (metal and pitch size), and the pad geometrical distribution. All these factors influence the spatial resolution.

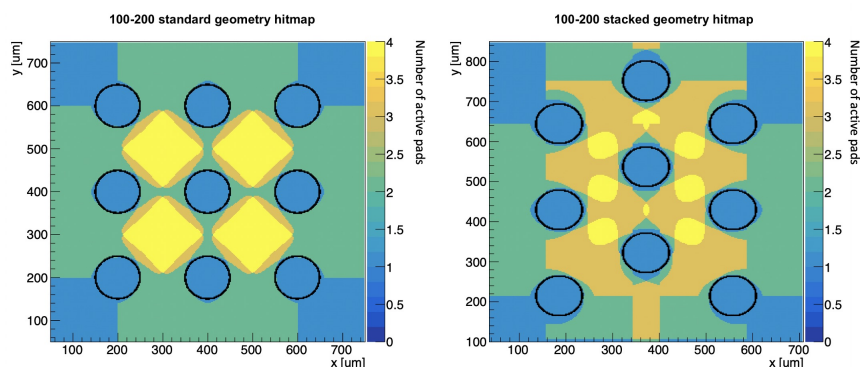


Figure 7: 2D maps representing how many pads see a signal depending on the hit position in a standard 3×3 100-200 pad-pitch matrix (left) and in a device with a modified layout (right). Black circles identify the edge of the metal pads, here computed as circles for simplicity.

For any given geometry, it is possible to identify how many pads see a signal. Figure 7 (left) shows an example of these calculation for a 3×3 100-200 matrix. The orange and yellow areas indicate the locations where hits can

be reconstructed with three or four pads respectively: information from at least three pads allows to uniquely identify the hit position and reach a very good spatial resolution. However, this geometry shows two shortcomings:

- When the pads are positioned at the corners of a square, as they are in this example, the reconstruction with three pads is less accurate since the hit tends to be reconstructed closer to the three active pads than it should.
- In the green area, only two pads record a signal and it is no longer possible to determine the hit position.

In order to obtain a detector with a very good and uniform spatial resolution, it is important to maximize the areas where the reconstruction is more precise. To this end, it is possible to optimize the disposition and shape of the metal pads. One such study is shown in Figure 7 (right): here, the AC pads are placed in a triangular geometry. This geometry has two advantages: the distance between every two pads is the same, and the optimum precision is obtained with only 3 pads, sufficient to reach full cluster efficiency.

3.4.1. Design of the metal pad

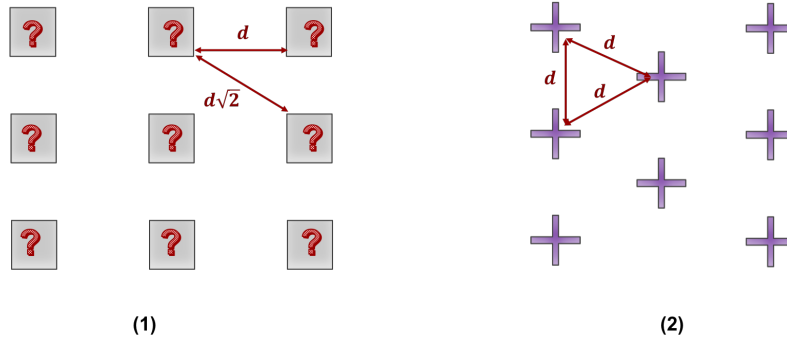


Figure 8: Present metal pads design in a 3×3 RSD matrix (1) and a possible optimization of the pads shape and disposition (2) considering there is no signal sharing when particles hit metal pads.

Both designs indicate that there is no signal sharing when the particle hits a metal pad. This property was measured with the laser by shooting the signal in a narrow slit without metal placed inside the metal pad. The measurements also showed that signal sharing happens when the hit is within

$\sim 10 - 20 \mu m$ from the metal edge. With this information, it is possible to redesign the metal pad to always have signal sharing. However, the new design should include two important aspects:

- The angle of view in Equation (4) should not be too small
- The capacitance of the metal pad should be large enough to prevent ballistic deficit.

Combining these aspects, Figure 8 proposes an optimization of the metal pad disposition.

4. Laser studies

The properties of the RSD sensors have been studied using the Transient Current Technique (TCT), which exploits the signal induced in the sensor by a laser. The TCT employed in this study, manufactured by Particulars, is equipped with an IR picosecond laser, with a minimum spot size of $\sim 10 \mu m$, and with a micro-metrical x-y moving stage. The intensity of the laser was set to reproduce the amount of ionization typical of a MIP in a sensor of the same active thickness, about 0.5 fC.

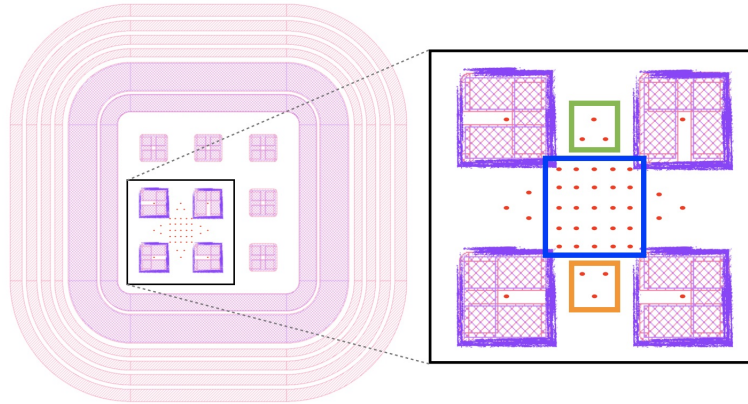


Figure 9: One of the sensors employed in the TCT set-up. The red dots represents the locations of the laser shots.

Several RSD matrices, with different combinations of pitch and pad sizes, have been characterized with the TCT setup. Each sensor has been tested at bias voltages corresponding to values of gain between 8 and 25. For each

matrix, the laser is shot in multiple points in the area among the pads, as shown in Figure 9. The four AC pads closest to the hit points have been read out simultaneously and their signals recorded using a 40Gs/s, 4 GHz BW oscilloscope. In every position, ~ 500 waveforms are acquired [8, 9, 11]. For each laser shot, the hit position is reconstructed using the method described in section 3.3. The spatial resolution at each position is evaluated as the sigma of the difference between the laser known coordinates and the reconstructed position $(x, y)_{reco} - (x, y)_{laser}$. Given that only four pads are read-out, only positions in which the whole signal is completely contained in these pads are considered in the following studies. These positions are marked by the blue square in Figure 9. Points between two pads, like the ones in the green and orange squares marked on the left side of Figure 10, are poorly reconstructed.

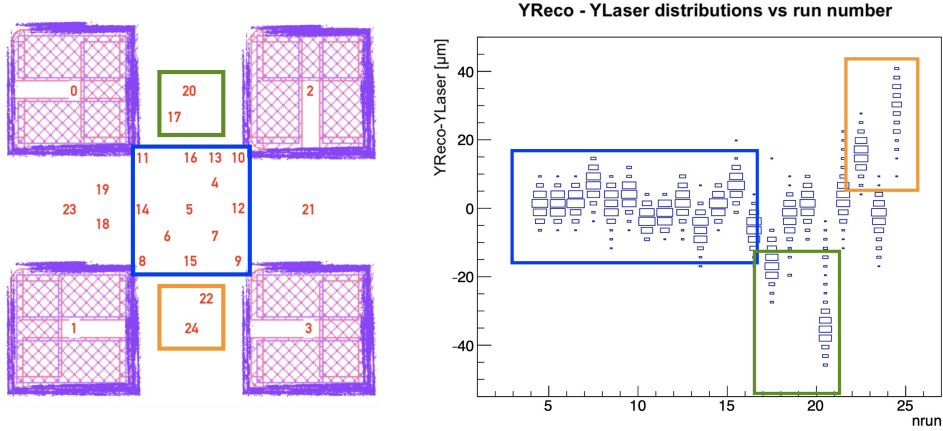


Figure 10: $y_{reco} - y_{laser}$ distributions plotted for single laser shots in different regions of the device.

For these areas, the 4 read-out pads miss part of the information and two more pads would be needed for a complete reconstruction. For this reason, as shown in the right plot of Figure 10, the $(x, y)_{reco} - (x, y)_{laser}$ distributions for these positions are wider and shifted.

Signals shot inside the metal opening of the pads suffer from even greater uncertainties, as the only information is the amplitude recorded by the only active pad. For this type of events, the spatial resolution corresponds to the case of binary read-out, $pad\ size/\sqrt{12}$.

4.1. Study of signal sharing among pads

TCT studies have also been used to verify the predictions of Equation (4). Figure 11 (a) displays the positions and the numbers of the laser runs included in the analysis for the 100-200 μm pad-pitch geometry. For each of these runs, the measured and predicted percentage of the amplitudes are compared in the plots (c)-(f) of Figure 11. On these 4 plots, the black points represent the calculated signals while the red points the measured values.

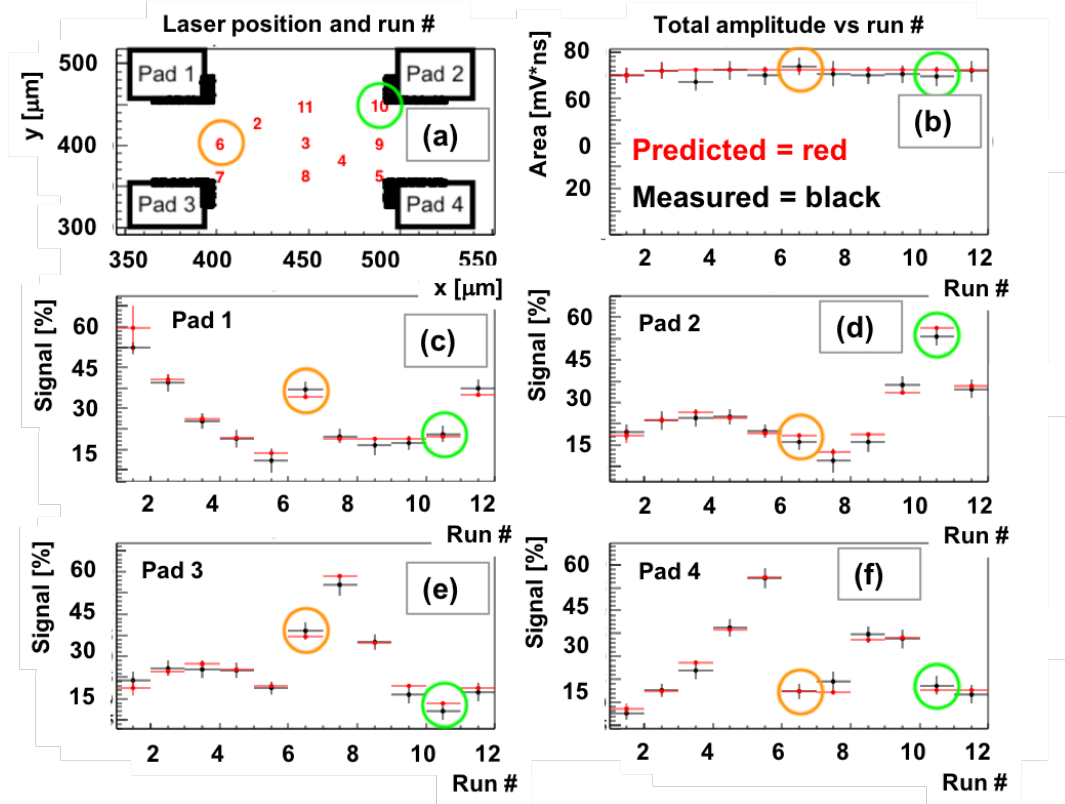


Figure 11: Map with positions of the laser runs for the 100-200 μm pad-pitch geometry (a); sum of the amplitude of the signals from the four read-out pad for each run (b). Plots (c)-(f) show the percentage amplitude seen by each AC pad as a function of the laser run number. Black points represent the predicted values obtained with the master formula, while the red ones are the measured amplitudes.

As an example, we consider run #6, highlighted with an orange circle in the figure. For this run, the amplitudes in both pads 1 and 3 are ~ 25 mV, as the laser is shot halfway between them, while pads 2 and 4 register smaller

signals, $\sim 10 - 15 \text{ mV}$, since they are farther from the run position. In contrast, in run #10, pad 2 sees most of the amplitude as the laser is shot as close as possible to its metal pad.

Additionally, in Figure 11 (b), the sum of the amplitude of the signals from the four read-out pads is plotted as a function of run number. This plot shows two interesting features: (i) the predicted and measured points are in agreement and (ii) the signal total amplitude is constant, regardless of the run position.

Overall, the RSD Master formula shows a very powerful predicting power, allowing to understand the dynamic of signal sharing.

4.2. Spatial resolution

Using the method explained in section 3.3, the spatial resolution has been computed as a function of the interpad distance for many geometries for both the MF and LA models. The results are shown in Figure 12. Several features are shown in the figure:

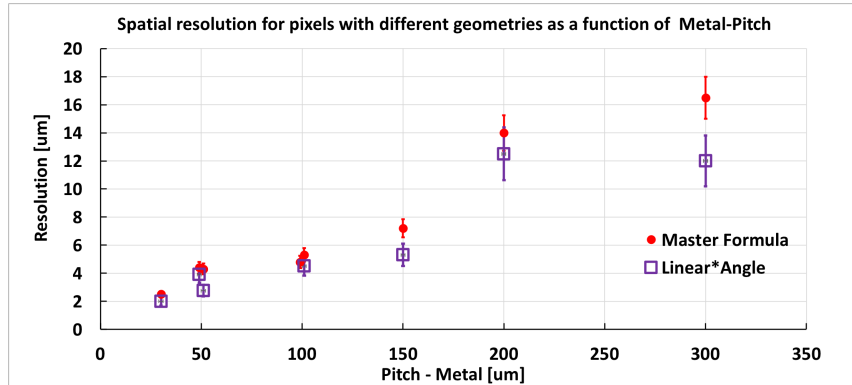


Figure 12: Spatial resolution for different RSD pad-pitch geometries as a function of the interpad distance obtained by reconstructing hit positions with both the MF (red points) and LA (purple squares) models.

- the spatial resolution is extremely good, less than $5 \mu\text{m}$ in both x and y direction for interpad distances up to 100-150 μm .
- smaller interpad distances yield better spatial resolutions.
- The MF and LA-tuned models yield similar results up to interpad of about 200 μm .

- For interpad distances above $200 \mu m$, the LA-tuned model yield better resolution. This discrepancy has been studied in detail, and the result confirmed. One possible explanation of this fact is that the MF assumes that the signal propagates on a cone: for larger distances, this fact might not be true anymore, leading to a degradation of its predictive power.

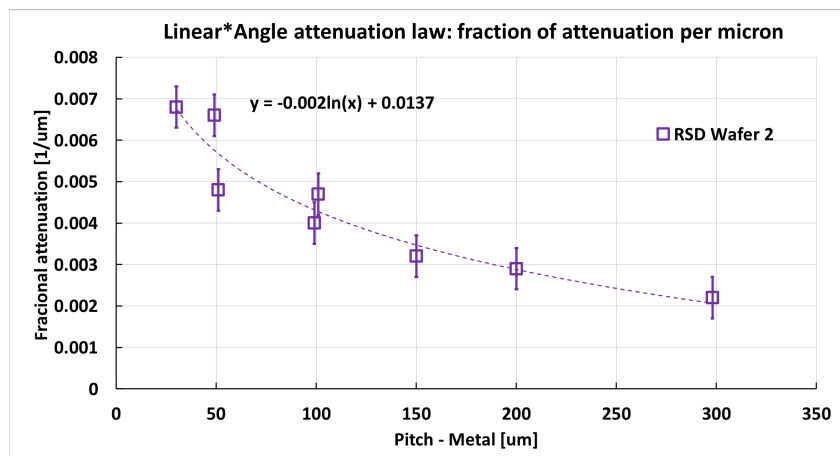


Figure 13: Optimum value of the attenuation factor β as a function of the interpad distance.

The results of the LA model shown in Figure 12 have been obtained tuning the parameter β (Equation (6)). For each measured pad-pitch geometry, the attenuation factor has been chosen as the one that minimizes the spatial resolution. The values of β parameters used in this analysis are presented in Figure 13 as a function of the interpad distance. The optimized β values have a logarithmic dependence on the length *pitch – metal*: this fact demonstrates that the attenuation with distance is logarithmic, as implemented in the MF. The same behaviour has been measured for the delay coefficient ζ of Eq.7, confirming that also the delay has a $\log(d)$ dependence. Both these aspects indicate that the resistance from the impact point to a pad is that of a triangular resistive surface.

The dependence of the spatial resolution upon the total signal amplitude has been studied for several pad-pitch geometries and it is shown in Figure 14. As expected, the resolution improves with amplitude, and the improvement is much stronger in larger geometries. For small geometries, the resolution

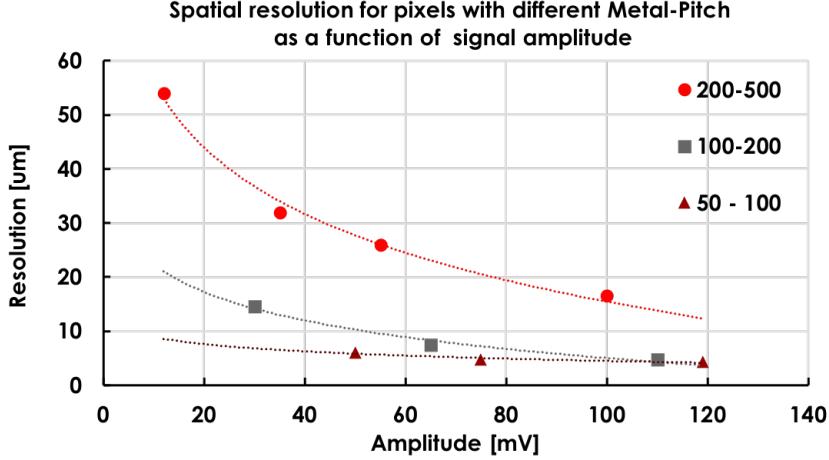


Figure 14: Spatial resolution as a function of signals amplitude for three pad-pitch geometries: 50-100, 100-200 and 200-500.

remains almost constant for a large range of amplitudes, showing that for these geometries even at low gain the performances are excellent.

One interesting point is to understand why smaller geometries perform better.

The position accuracy of an RSD sensor can be parametrized as the sum of three contributions:

$$\sigma_{tot}^2 = \sigma_{jitter}^2 + \sigma_{algorithm}^2 + \sigma_{sensor}^2. \quad (9)$$

- σ_{jitter} : this term represents the spatial uncertainty due to the electronic noise $\sigma_{el_{noise}}$. Consider two RSDs with different interpad distances: 100 μm and 300 μm . Consider also a simplified RSD sensor, with only 2 pads. In this case, a pad records the maximum signal amplitude (assumed to be 100 mV) when the signal is very near, and a null amplitude when the signal is near the other pad. The amplitude as a function of pad-hit distance for the two geometries is shown in Figure 15.

In the 100 μm geometry, the amplitude changes by $dV/dx = 1 \text{ mV}/\mu m$, while in the 300 μm geometry by $dV/dx = 0.3 \text{ mV}/\mu m$. The effect of the electronic noise is to change the amplitude by $\sigma_{el_{noise}}$, creating an uncertainty in the localization given by

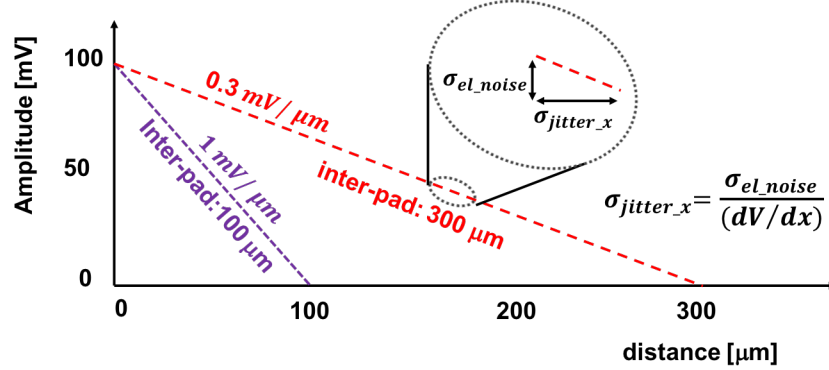


Figure 15: Amplitude as a function of distance for two RSD geometries. The jitter is worse for larger structures.

$$\sigma_{jitter} = \frac{\sigma_{el_{noise}}}{\frac{dV}{dx}} = \frac{\sigma_{el_{noise}}}{\frac{Amplitude}{Interpad}} \quad (10)$$

Assuming $\sigma_{el_{noise}} = 3 \text{ mV}$ (the noise in our setup), the jitter term for the $100 \mu\text{m}$ case is about $\sigma_{jitter} = 3 \mu\text{m}$, while it becomes $\sigma_{jitter} = 10 \mu\text{m}$ for the larger structure.

- $\sigma_{algorithm}$: the reconstruction code uses algorithms to infer the hit position from the measured signals. This can be done analytically, using a lookup table, or with more advanced techniques such as machine learning [10]. In all cases, the method selected has a given accuracy (whose impact has been mentioned in relation to Figure 12);
- $\sigma_{sensors}$: this term groups all sensor imperfections contributing to an uneven signal sharing among pads. The most obvious is a varying n+ resistivity: a 2% difference in n+ resistivity will turn an equal split between two pads, say 50 mV each, into 49 mV and 51mV, respectively, yielding $\sigma_{sensors} \sim 1 \mu\text{m}$ for the $100 \mu\text{m}$ geometry and $\sigma_{sensors} \sim 3 \mu\text{m}$ for the $300 \mu\text{m}$ design.

In light of this parametrization, the values shown in Figure 14 indicate that the spatial resolution of the largest structure (200-500) is completely dominated by the jitter term. For the two smaller geometries, the resolution becomes constant at high amplitude: in this region, the jitter term becomes

subleading, and the resolution is dominated by the uncertainties due to the sensor and/or reconstruction algorithm.

Figure 12 shows clearly the effect of the term $\sigma_{algorithm}$ for the MF and LA methods: for interpad distances up to 150-200 μm , the two methods yield to similar resolutions, while for the 300 μm geometry the LA method is better. This difference indicates that on large distances the propagation does not happen with a triangular shape, as postulated by the master formula and the MF algorithm becomes less precise.

4.3. Temporal resolution

Once the impact position has been reconstructed, the time of the hit is evaluated in a 2-step process. First, the time measured in each pad is corrected by the propagation delay from the impact position to the pad metal edge using Equation (5). The value of the γ parameter of Equation (5) is tuned to obtain the best resolution.

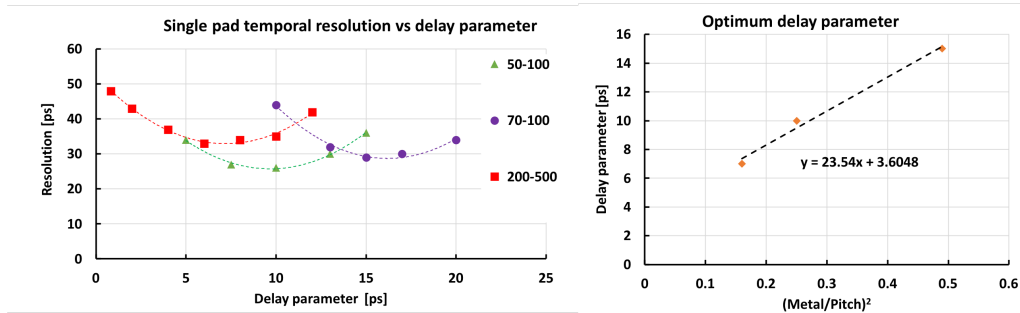


Figure 16: Left side: Single pad temporal resolution as a function of the delay parameter for three pad-pitch geometries: 50-100, 70-100 and 200-500. Right side: Optimum delay parameter as a function of the ratio $(metal/pitch)^2$.

The left part of Figure 16 shows how the temporal resolution of a single pad changes as a function of the delay parameter for three different geometries from the same wafer. As the right side of Figure 16 shows, the optimum delay parameter depends linearly on the ratio $(metal/pitch)^2$. This fact is an indication that the geometrical properties of a given design, and not just the n^+ resistivity, play a role in the delay.

Then, the time of the event is defined as the amplitude-weighted time average of the active read-out pads. The temporal resolution is obtained as the sigma of the $t_{trigger} - t_{reco}$ distribution. An example of these steps is

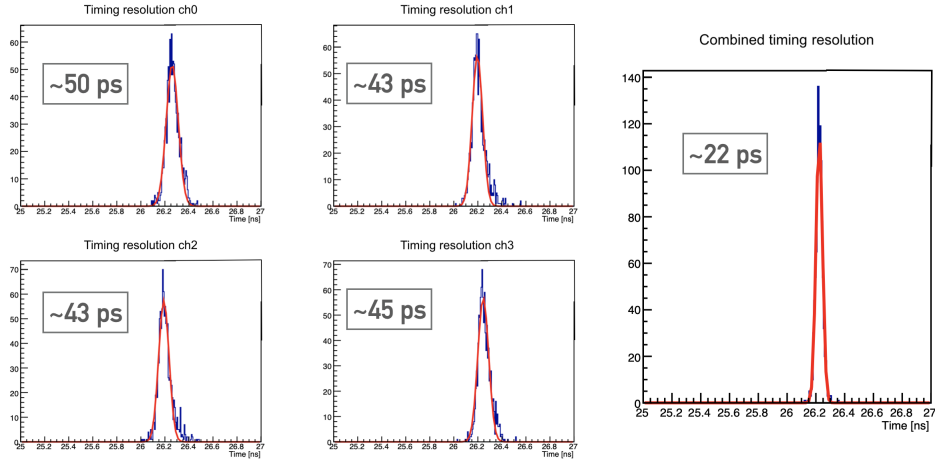


Figure 17: On the left: single-channel temporal resolution for the four read-out pads for laser data. On the right: total temporal resolution obtained combining the four pads timestamps.

shown in Figure 17: the left side shows the temporal resolution of each of the 4 active pads for the 100-200 geometry, while on the right the combined resolution. The resolution of the single channel is about ~ 45 ps, while the combination of the 4 channels yields to about ~ 22 ps, as expected from a situation without correlated noise (22 ps ~ 45 ps/ $\sqrt{4}$).

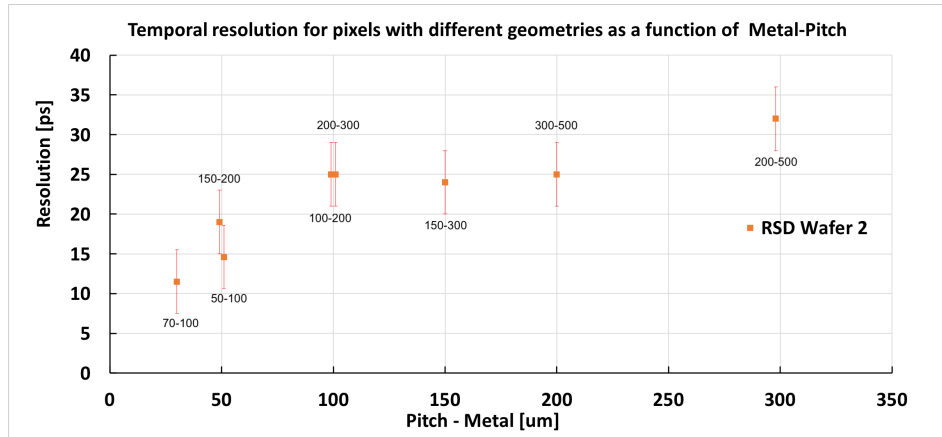


Figure 18: Temporal resolution for different RSD pad-pitch geometries as function of the interpad distance.

The temporal resolution as a function of the interpad area is shown in Figure 18. The resolution increases up to $pitch - pad = 100 \mu m$. For interpad larger than $100 \mu m$ the trend flattens, stabilizing around $25 - 30 ps$.

4.4. Summary of laser results

The spatial and temporal resolutions obtained for each geometry are summarized in Table 1.

pad-pitch geometry	spatial resolution [μm]	temporal resolution [ps]
50-100	4.3	14.7
70-100	2.5	11.5
100-200	4.8	25
150-200	4.4	19
150-300	7.2	24
200-300	5.3	25
200-500	16.5	32
300-500	14	25

Table 1: Spatial and temporal resolutions from TCT measurements for different RSD pad-pitch geometries. These results refer to studies where the laser has been shot in the interpad region of the sensors, as shown in Figure 9

The temporal resolution is in line with the best LGAD results, demonstrating how the RSD design does not degrade the LGAD performances. The RSD spatial resolution is extremely good for all geometries as the reconstruction method is able to exploit the power of internal signal sharing.

5. RSD simulation in Weightfield2

Weightfield2² is a simulation program that has been extensively used in the design and characterization of the LGAD properties [12]. WF2 emulates the passage of a particle in a silicon detector and generates the output current, including the effect of non-uniform ionization, gain, geometry, and acceptor removal. The RSD principle of operation has been added to the WF2 program by implementing the prediction of the RSD master formulas, Equations (4) and (5). In WF2-RSD it is possible to select a given pad geometry and to simulate the current signals in the nearby pads as a function

²Shareware at <http://cern.ch/nicolo>

of the hit position. Figure 19 shows on the left an example of geometry, and indicated by the purple circle the position of the hit. The number near each pad is the fraction of signal seen in that pad. On the right side, the shape of the DC current, of the total AC current, and the currents in each of the pad is shown. The program allows generating many events in batch mode and writing the events to a file for offline analysis.

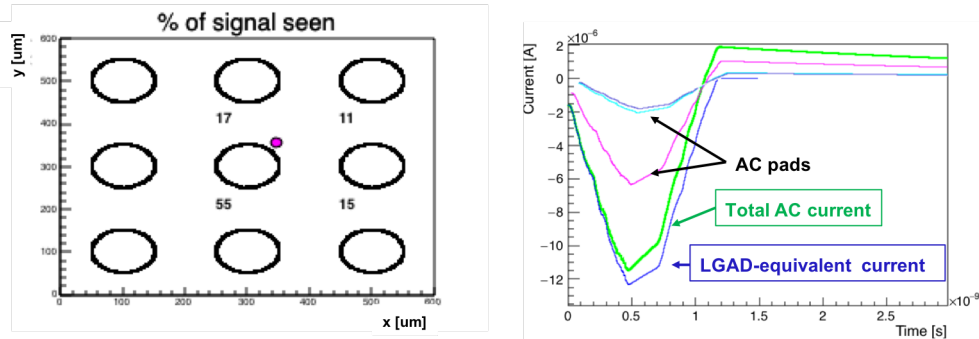


Figure 19: An example of pad geometry and of the current signals simulated by WF2-RSD.

6. Test Beam measurements

Two 3×3 RSD matrices from the same wafer, with 100–200 and 190–200 pad-pitch geometry, operating at -430 V, were measured at the Fermilab Test Beam Facility. In this facility, 120 GeV/c protons are delivered every minute in 4 seconds spills, each containing 50-100k particles. RSDs were mounted to a block cooled by circulating glycol that enables holding the sensor at a constant temperature of $(22 \pm 0.1)^\circ\text{C}$. They were wire-bonded to a 16-channel read-out board, designed at Fermilab. The 16-channel board is designed to test sensors with sizes as large as 8.5×8.5 mm² at voltages up to 1 kV. Up to sixteen sensor outputs can be wire-bonded to the input pads of 2-stage amplifier chains based on the Mini-Circuits GALI-66+ integrated circuit. In this particular configuration amplifiers used a 25Ω input resistance, a ~ 5 k Ω total transresistance, and a bandwidth of 1 GHz. The box containing the device under test (DUT) was preceded by a tracking telescope, approximately 2 meters upstream along the beamline. The tracking system was provided with 14 layers of strips and 4 layers of pixels, and followed by two additional strips layers. In this configuration, the tracker provides a spatial resolution of $\sim 45 \mu\text{m}$, somewhat degraded by the extrapolation downstream and by

material between the telescope and the DUT. Additionally, the setup was instrumented with a Photek 240 micro-channel plate detector, placed inside the environmental chamber after the DUTs, with a temporal resolution better than 10 ps [13].

The data were acquired with a Keysight MSOX92004A 4-channels digital scope with 40 GS/s and 20 GHz analog bandwidth. Given that only 4 signals could be recorded simultaneously, different types of datasets were recorded:

- 4 AC pads,
- 3 AC pads and the Photek [14],
- 2 AC pads, the DC pad and the Photek.

The following quality cuts were required in the analysis:

- the presence of only one isolated proton per event in the tracking system; its track must have hits at least in 14 layers of the tracking telescope and in one of the two downstream strip layers.
- the signal on each RSD read-out pad has to be larger than 15 mV,
- the signals should not saturate the scope
- the sum of the AC signals has to be larger than 80 mV (60 mV) when read with 4 (3) pads.

6.1. 100 – 200 *geometry: 4-pads configuration studies*

Since the tracker resolution, approximately 45 μm , is large compared to the RSD resolution, it is not possible to perform a simple comparison of the tracker and RSD positions event by event.

Using the selection cuts above, Figure 20 reports the hit position using the the tracker (left), the MF (center), and LA (right) models. Given the worse resolution, the area covered by the hits is larger when using the tracker, while MF and LA predict similar distributions. Given that the beam test illuminates uniformly the DUT, the density of hits as a function of position is constant. However, the measured distribution includes the reconstruction smearing. This effect is shown in Figure 21, where the events in the y-range $23255 \mu m < y < 23345 \mu m$ are plotted versus the x-axis. For the tracker case, given the rather large resolution, the distribution is not flat. On the

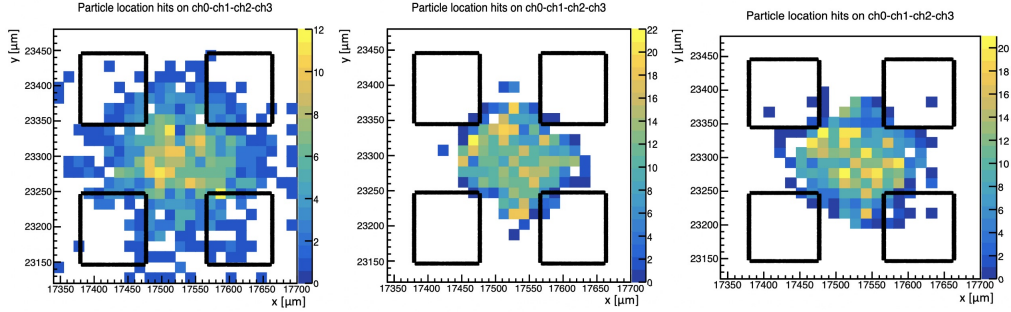


Figure 20: Hit maps for the 100-200 geometry represented using the tracker coordinates (left) and reconstructed with the analytical method using the MF (center) and LA (right) models.

other hand, both the MF and LA methods show a good spatial uniformity for reconstructed events, showing that the smearing introduced by the analytical method is small.

Even though an event-by-event comparison between the tracker and the RSD reconstruction cannot be done, a comparison between mean values is possible. Figure 22 shows, for three x-y intervals, where the tracker reconstructed positions are (red points) when selecting the events using the RSD position (blue points).

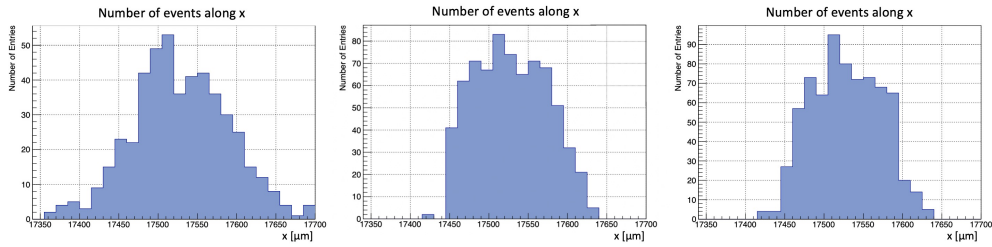


Figure 21: Number of events represented as a function of x-coordinate in the range $23255 \mu\text{m} < y < 23345 \mu\text{m}$ for the tracker (left), the MF (center) and LA (right) models.

This study is further investigated in Figure 23, where $y_{tracker}^{mean}$ is plotted as a function of y_{RSD}^{mean} . For each point, the events are selected by requiring their RSD position to be within an x-y square of $30 \times 30 \mu\text{m}^2$. Both MF (left) and LA (right) models work very well, the correlation factors R^2 and the fit slope are close to 1.

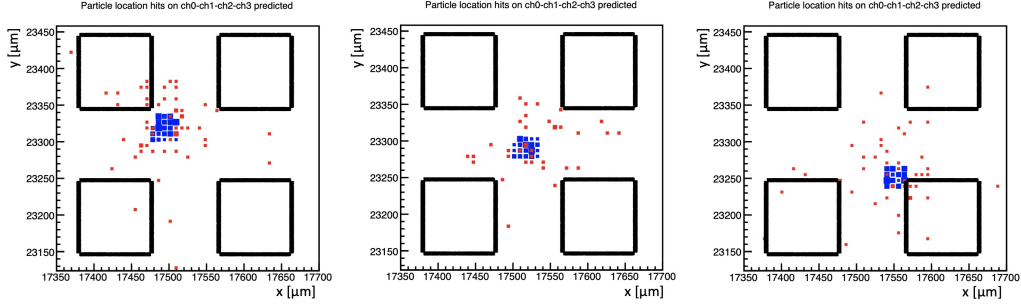


Figure 22: Hit maps comparing hit positions defined by RSD coordinates (blue) and the tracker ones (red) for events selected in $30 \times 30 \mu\text{m}^2$ defined by the RSD coordinates in the interior of the 4 pads.

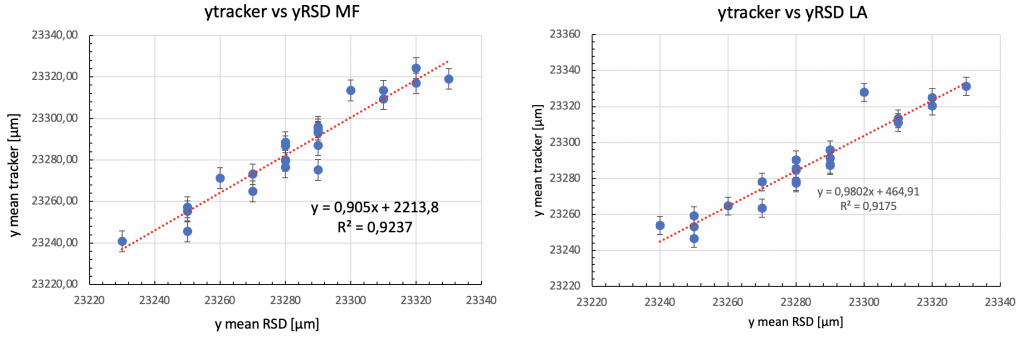


Figure 23: $y_{tracker}^{mean}$ plotted as function of y_{RSD}^{mean} for the MF (left) and the LA model. The parameters resulting from the linear fit are displayed on the plots.

This result proves that the MF model can accurately reproduce experimental data despite the absence of tunable parameters. In the LA model, it is instead necessary to optimize the attenuation factor β , whose best value in these studies is $\beta = 0.003/\mu\text{m}$.

6.1.1. Spatial resolution using signals from 3 or 4 pads

In the dataset used for timing measurements, only 3 AC pads can be used for hit reconstruction. The analysis presented in the previous section is thus repeated including only 3 pads to compare 4- and 3-pads spatial resolutions. If we consider events in a triangular area near the included pads, the spatial resolution for the 3-pads dataset is equal to the 4-pads one. Moving to the total device area, the spatial resolution worsens since the information from

the missing pad would be needed to define the hit positions more accurately

6.2. 100 – 200 geometry: timing studies using 3 AC pads and the Photek detector as time reference

The first step in the timing analysis is to measure the propagation delay, from the hit point to the read-out pads. The hit positions are reconstructed using the MF model.

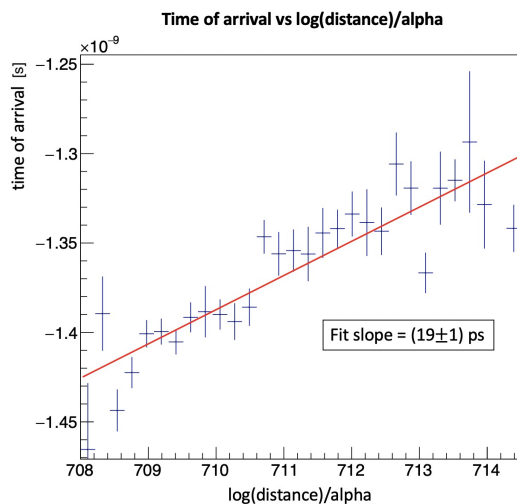


Figure 24: Time of arrival of the 100-200 3-pad configuration as a function of $\frac{\log(d)}{\alpha}$.

Two methods are used to extract the best time delay parameter γ (Equation (5)).

- In the direct method, the time of arrival is plotted as function of $\frac{\log(d)}{\alpha}$ and fitted linearly: the fit slope represents the time delay parameter, that is here $\gamma_{dir} = (19 \pm 1) ps$ (Figure 24).
- The second method finds the time delay indirectly by minimizing the temporal resolution as a function of the delay parameter, as shown in Figure 25. For each pad, the best γ parameter is the one that minimizes the temporal resolution. The resulting values are $\gamma_{CH0} = (12.1 \pm 0.6) ps$, $\gamma_{CH1} = (17.0 \pm 0.1) ps$, and $\gamma_{CH2} = (19.5 \pm 0.2) ps$.

The delay value used in the analysis is the mean of the four results from the two methods while as uncertainty the $(\max-\min)/2$ is used $\gamma = (16.9 \pm 3.7) ps$.

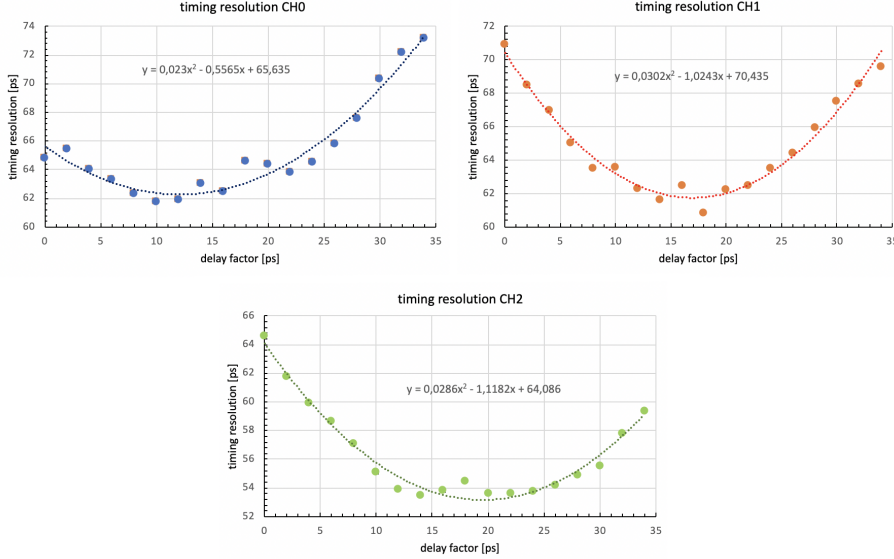


Figure 25: Time resolution represented as a function of time delay parameter γ for the three RSD channel of the 100-200 3-pads configuration.

6.2.1. Temporal resolution results

Once the delay parameter has been evaluated, the signals from the 3 pads can be combined to form t_{RSD}^a , defined as the arithmetic mean of their times of arrival. The temporal resolution is measured as the sigma of the distribution of $t_{RSD}^a - t_{Photek}$. Figure 26 shows the three single-channel resolutions (top) and the combined one (bottom), $\sigma_{tot} = (51.9 \pm 0.5) ps$. In contrast to the laser results (Figure 17), this value is higher than the one expected by combining the three single-channel resolutions assuming uncorrelated pads ($\sim 34 ps$). This is caused by the presence of a correlated noise due to non-uniform ionization.

The temporal resolution has two terms, one depending on the non-uniform ionization [15] and the other due to jitter.

$$\sigma_{tot}^2 = \sigma_{Jitter}^2 + \sigma_{ionization}^2$$

The only contribution to the laser temporal resolution is $\sigma_{jitter} = \frac{\sigma_{elnoise}}{dV/dt}$, where $\sigma_{elnoise}$ is the electronics noise of each read-out channel. This contribution, in our setup, is uncorrelated among channels. In the test beam, σ_{tot} also includes the contribution of non-uniform ionization. This contribution is fully correlated among pads: in RSDs, the signals spread from the hit

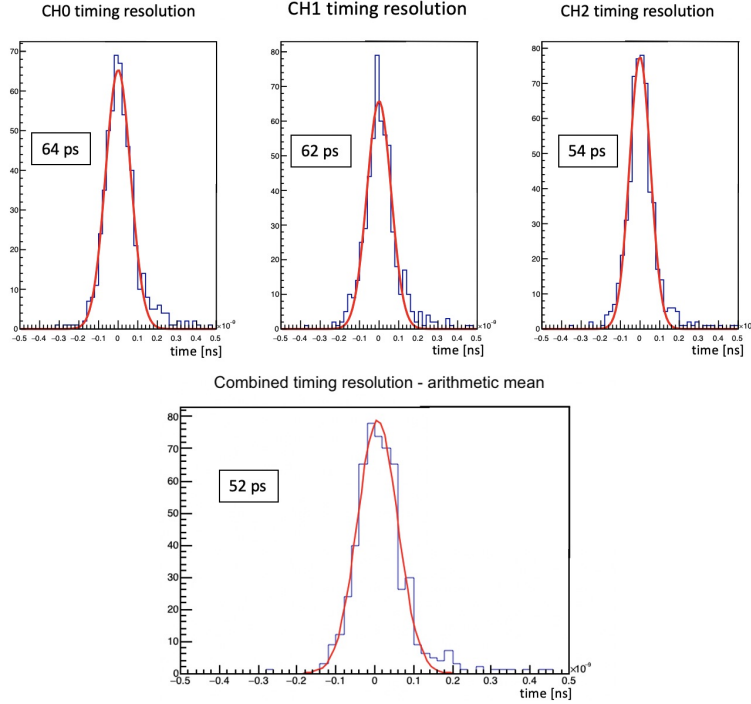


Figure 26: Top: single channel temporal resolution for the three read-out pads at test beam. Bottom: total temporal resolution obtained as the arithmetic mean of the three pads timestamps.

point to the AC pads, and each pad sees a copy of the same signal. As a consequence, the jitter term is reduced by combining RSD signals, but the non-uniform ionization is not since it depends on the shape of the initial signal.

The reconstruction of the hit position thus greatly benefit from signal sharing among pads, whereas temporal resolution does not improve using multiple pads as the shapes of the signals are largely correlated.

In the $t_{RSD}^a - t_{Photek}$ in Figure 26 (bottom), t_{RSD} is calculated as the arithmetic average of the three RSD timestamps. This result can be improved if t_{RSD} is instead calculated as an amplitude-weighted average, t_{RSD}^w , yielding to a temporal resolution of $t_{RSD}^w = (44.4 \pm 0.3) ps$ (Figure 27). This value is in line with the best LGAD performances obtained at the same gain and using the same electronics. The effect of amplitude weighting is to reduce the importance of small signals, where the signal-to-noise ratio is worse.

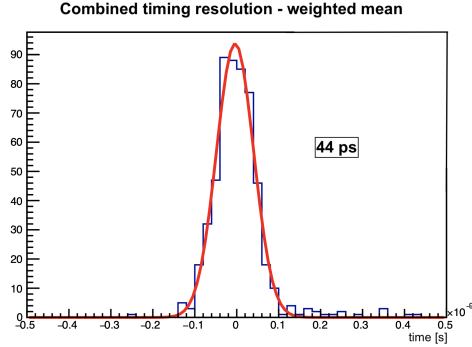


Figure 27: $t_{RSD} - t_{Photek}$ distribution with t_{RSD} calculated as the amplitude-weighted mean of the three pads timestamps.

6.3. 190-200 geometry: 3 AC pads and the Photek

The 190-200 geometry was used to study the effect of large metal pads and floating electrodes on the signal reconstruction.

6.3.1. Position reconstruction and the effect of floating pads

Figure 28 shows the normalized density and position of hits reconstructed by the tracker when pad 1 (left side) or 2 (right side) is active.

Pad 1, shown on the left side of 28, has 4 floating neighbours, pads A, B, C, and D and four grounded neighbours, pads 0, 2, 3, and 4. Clearly, when the particles hit a floating pad, the signal is well visible in pad 1. In contrast, when particles hit a grounded pad there is not signal sharing. The right side of Figure 28 shows the same situation for pad 2: here all neighbours are grounded: hits are visible only when they directly occur on the pad.

These two plots confirm that floating pads do not contribute to signal sharing, while when the impact point is on a grounded pad, there is almost no sharing.

For the same two AC pads, Figure 29 shows the signals amplitude as a function of x-coordinates. Pad 1 (left) is between a grounded pad and a floating one, while pad 2 (right) is placed between a grounded pad and the device edge. Amplitude attenuation is steeper next to grounded pads than underneath the floating ones.

These plots highlight how RSD signals with large metal pads work differently with respect of RSD with small metal pads:

- Most of the events are seen by only one pad

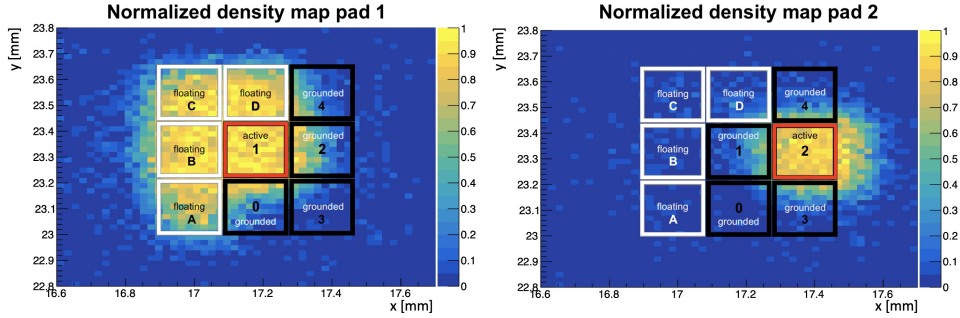


Figure 28: Normalized density maps for pad 1 (left) and pad 2 (right) of the 190-200 geometry. The red square is the read-out pad, black squares indicate grounded pads, while the white ones represent the floating pads.

- Signal sharing is limited in a very narrow region between pads.
- RSDs with large metal pads are similar to traditional LGADs, benefiting from a design that provides 100% fill factor.

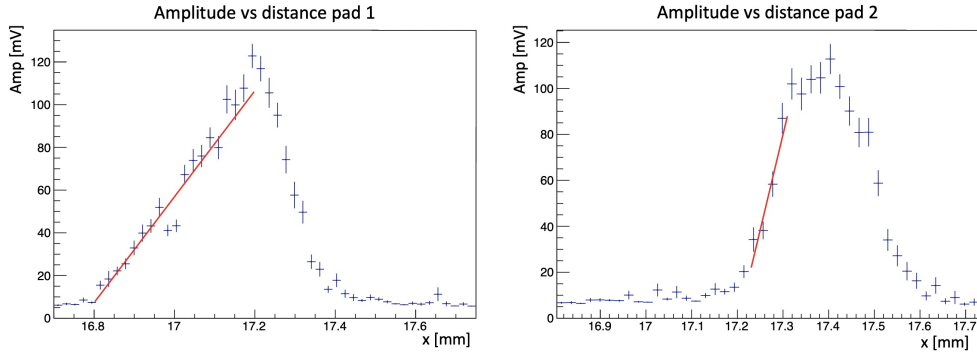


Figure 29: Amplitude along x axis for pad 1 (left) and 2 (right): the first is amidst a grounded and a floating pad, while the second is between a grounded pad and the sensor edge.

For this reason, in this dataset, the large majority of events is seen only by one of the read-out pads, and 2- and 3-pads events are very few. Hit reconstruction is thus not applied to the 190-200 matrix, and the spatial resolution is estimated as $pad\ size/\sqrt{12}$ ($\sim 55\ \mu m$).

6.3.2. Temporal resolution

As a consequence of very limited signal sharing, the temporal resolution of this geometry is very good for 1-pad events (very small jitter since the signal is large) and slightly worse for the 2-pads events. For the timing analysis, the selection cuts are:

- the sum of the AC signals is required to be larger than 80 mV,
- the signal on each pad should be larger than 15 mV,
- the tracker coordinates of the events need to have $x > 17.05 \text{ mm}$ and $y < 23.45 \text{ mm}$.

With this selection, the following temporal resolution was obtained:

- 1-pad events: ($\sigma = 32 \pm 1$) *ps*
- 1-, 2- and 3-pads events: ($\sigma = 42.1 \pm 0.6$) *ps*.

Overall, RSD sensors with the AC metal pads of about the same geometry of the pitch offer excellent temporal resolution, and a 100% fill factor. They are a good choice when the position resolution offered by (pixel size)/ $\sqrt{12}$ is enough.

6.4. 100-200 geometry: DC pad studies

As explained in Figure 3, the signal is formed on the n^+ electrode. In this section, the properties of this signal are analyzed by concurrently reading the current from two AC pads and the n^+ (DC) contact. This study has identified two different families of events, depending the impact point on the RSD (Figure 30):

- If the impact point is between the edge of the sensor and the first column of metal AC pads, both the DC (blue) and AC (red) signals have a fast component.
- In contrast, when the particle hits the RSD anywhere among the AC pads, the DC signal does not show a fast component.

This difference happens because the fast component always follows the path with the lowest high-frequency resistance to ground: when the particle hits among AC pads, this is represented by the AC ground. However, when

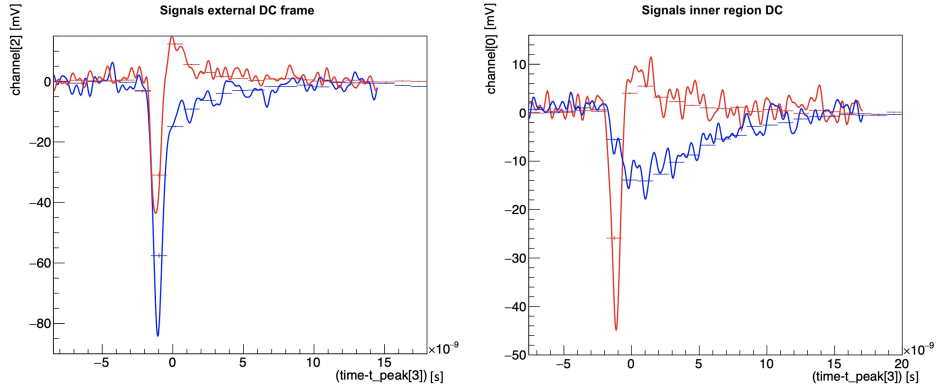


Figure 30: Signals recorded by the DC pad (blue) and the closest AC pad (red) in the external DC frame (left) and in the inner DC region (right). The solid lines are a single pulse, while the average on few tens of waveforms is represented with markers.

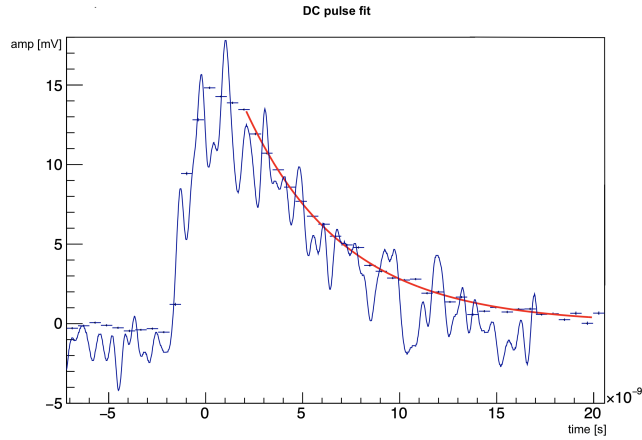


Figure 31: The average of a hundreds of DC signals (markers) selected in the DC pad inner region and fitted with an exponential function to measure the RC time constant (red line). An example of a single pulse is represented in a solid blue line.

the particle hits near the edge, the DC contact is sufficiently low resistance to absorb part of the fast signal.

In both regions, the falling edge of the pulse depends on the AC discharge current.

The RC time constant of the DUT can be obtained by fitting the falling edge of DC signals with the exponential function $e^{-\frac{t}{RC}}$ (Figure 31). The resulting RC value for this geometry is $(5.08 \pm 0.03) ns$.

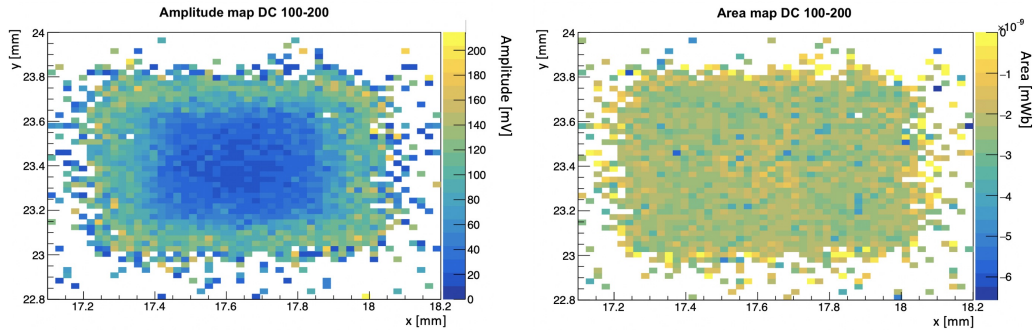


Figure 32: On the left, the amplitude map for the DC pad shows a difference in amplitude between the inner region and the external frame, while the map on the right shows a constant behaviour for signals area.

The amplitude of the DC signal as a function of position is displayed in the 2D map in Figure 32 (left): pulses near the edge, due to the presence of the fast component, have a much larger amplitude. Figure 32 (right) shows instead the pulse area, that remains constant.

6.5. 100-200 geometry: timing properties of the DC pad signals

Figure 33 shows that signals in the center of the DC pad are recorded with a time delay compared to the ones on the external frame. This delay represents the signals propagation time towards the DC contact.

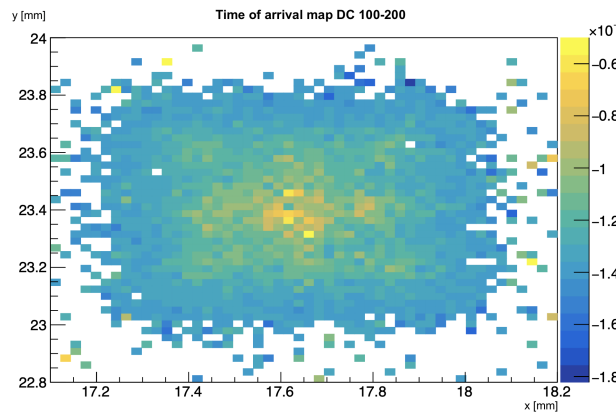


Figure 33: Time of arrival map: signals generated in the center of the DC pad are delayed with respect to the one on the external frame.

Given that only the signals near the edge have a fast component, the temporal resolution can be obtained only for that specific region. These signals are selected applying a cut on the amplitude of at least 60 mV. The temporal resolution for this region is (45.1 ± 0.7) ps, in agreement with the values obtained combining the AC pads resolutions presented in the previous sections.

7. Conclusions

This paper presents the principles of operation of Resistive AC-Coupled Silicon Detectors, a new type of LGAD characterized by a continuous gain layer and an AC-read-out design. RSDs are the first silicon detector with internal signal sharing. Thanks to the RSD design, signals are spread among the neighbouring pads, allowing for a very precise determination of the hit position. The paper presents laser and beam test analyses to determine the RSDs performances. A spatial resolution of less than $5 \mu m$ is achieved with large pixels ($\sim 100 \mu m$) with a temporal resolution of ~ 40 ps.

Acknowledgment

We kindly acknowledge the following funding agencies and collaborations: INFN - Gruppo V; Horizon 2020, grant UFSD 669529; Dipartimenti di Eccellenza, Università degli Studi di Torino (ex L. 232/2016, art. 1, cc. 314, 337); Ministero della Ricerca, PRIN 2017, progetto 2017L2XKTJ 4DInSiDe. Ministero della Ricerca, FARE, progetto R165xr8frtfare.

References

- [1] N. Cartiglia, et al., Issues in the design of ultrafast silicon detectors [online] (Tredi2015).
- [2] N. Cartiglia et al., “Silicon sensors for future particle trackers,” HSTD12, Hiroshima, Japan, 2019.
- [3] M. Mandurrino et al., “Demonstration of 200-, 100-, and 50- μm pitch Resistive AC-Coupled Silicon Detectors (RSD) with 100% fill-factor for 4D particle tracking,” IEEE Electron Device Letters, vol. 40, no. 11, pp. 1780-1783, November 2019.

- [4] M. Mandurrino et al., "Analysis and numerical design of Resistive AC-Coupled Silicon Detectors (RSD) for 4D particle tracking," NIM A, Vol. 959, 163479, 2020.
- [5] G. Giacomini, W. Chen, G. DAMen, A. Tricoli, "Fabrication and performance of AC-coupled LGADs," JINST 14 (09) (2019) P09004.
- [6] N. Cartiglia, M. Mandurrino, "Innovative silicon sensors for future trackers," CERN EP Detector Seminar, June 2020.
- [7] N. Cartiglia, "Signal formation and design optimization of Resistive AC-LGAD (RSD)," TREDI, Wien, February 2020.
- [8] R. Arcidiacono et al., "State-of-the-art and evolution of UFSD sensors design at FBK," HSTD12, Hiroshima, Japan, 2019.
- [9] G. Paternoster et al., "Novel Strategies for Fine-Segmented Low Gain Avalanche Diodes," HSTD12, Hiroshima, Japan, 2019.
- [10] F. Siviero, "Use of machine learning algorithms for the signal reconstruction of Resistive Silicon Detectors", submitted to JINST, 2020.
- [11] M. Tornago, "Characterization of the first RSD production at FBK," 35th RD50 Workshop, CERN, Geneva, November 2019.
- [12] F. Cenna et al., "Weightfield2: A fast simulator for silicon and diamond solid state detector, NIMA 796 (2015) 149-153.
- [13] A. Apresyan et al., Measurements of an AC-LGAD strip sensor with a 120 GeV proton beam, submitted to JINST, 2020.
- [14] M. Tornago, "Latest results on RSD spatial and timing resolution," 36th RD50 Workshop, CERN, Online Workshop, June 2020.
- [15] H. F.-W. Sadrozinski, A. Seiden and N. Cartiglia, "4D tracking with ultra-fast silicon detectors", Reports on Progress in Physics, vol. 81, no. 2, 2018.